



A novel rapid methodology for generating bilayer base-flow solutions involving surface patterning

Markus Scholle^{1,a} , Philip H. Gaskell², Sara Ismail-Sutton², and Marcel Mellmann¹

¹ Institute for Flow in Additively Manufactured Porous Media (ISAPS), Heilbronn University, Max-Planck-Straße 39, 74081 Heilbronn, BW, Germany

² Department of Engineering, Durham University, Stockton Road, Durham DH1 3LE, UK

Received 27 June 2024 / Accepted 13 December 2024
© The Author(s) 2025

Abstract Two bilayer flow arrangements, involving either (i) shear- or (ii) gravity-driven fluids, are explored in the presence of a periodically repeating surface topography. Key simplifying assumptions are that the flow is considered two-dimensional and inertialess. The solutions are obtained utilising a novel first-integral representation of the Navier–Stokes equations, leading to a highly efficient methodology for generating the accompanying flow structure within the layers in tandem with the disturbance experienced by the internal interface separating them—for configuration (ii) this extends also to the upper layer’s free-surface shape. Representative examples of each flow type, with a change of key parameters, are provided with particular emphasis on (ii).

1 Introduction

Gravity-driven single layer, steady film flow over a rigid substrate containing surface topography has been a topic of considerable research interest over the past four decades. The industrial motivation being the need to minimise, ideally avoid, any subsequent lack of planarity and resultant optical defects in the finished protective or functional coated layer applied. It is arguably the early work of Stillwagon and Larson [1], concerning the use of spin-coating driven by a centrifugally generated body force, that spawned the subsequent research efforts addressing the simpler problem of gravity driven film flow directed at unravelling the impact of the presence of unwanted micro-scale surface features, such as an isolated dust particle considered by Decré and Baret [2], or extensively printed electronic circuitry explored by Lee et al. [3].

It is only latterly that related interest has emerged for problems when such flows involve two or more superposed adjacent immiscible liquids. A long wave approximation, extendable to any number of layers, was used by Abdalla et al. [4] to explore numerically the disturbance the internal separating interface and free-surface experience when a bilayer film encounters steep-sided topographical surface features. Recent associated work of note, but in the absence of surface topography, is that of Thompson and Blyth [5] and Alexander and Papageorgiou [6] investigating the stability and dynamics of inertialess multilayer film and channel flow, respectively. The focus of the contribution reported here is the efficient generation of inertialess steady-state, base-flow bilayer solutions, useful for subsequent stability analyses, influenced by the presence of a periodically patterned substrate. Beginning with shear-driven flow, having direct tribological applications related to artificial replacement joints as reported by Qiu et al. [7], Basri et al. [8], Nečas et al. [9] and the beneficial use of surface texturing in this context demonstrated by Gachot et al. [10], Chyr et al. [11]; followed, but with a greater attention directed at gravity-driven, free-surface film flow over both weak and strong surface undulations, due to its broad relevance in coating technology—see Kistler and Schweitzer [12].

The paper is structured as follows. Section 2 provides details of the overall problem specification which, to set the scene, is followed by a brief review of the underpinning potential based variational approach for the general case of three-dimensional (3D) steady flow. The particular case of two-dimensional (2D) bilayer inertialess (Stokes) flow is

Markus Scholle, Philip H. Gaskell, Sara Ismail-Sutton and Marcel Mellmann contributed equally to this work.

^a e-mail: markus.scholle@hs-heilbronn.de (corresponding author)

then addressed, where the governing PDEs are formulated for the first time as Euler–Lagrange equations from the variational principle and boundary/interface conditions. Section 3 provides a description of their rapid method of solution involving transformation to complex variables; it is comprised of a brief description of the semi-analytic complex variable (CV) approach adopted, followed by its novel formulation for bilayer flow, before continuing with an outline of the related spectral discretisation employed. Two complementary additional methods of solution are considered next: an analytic first integral formulation together with high-fidelity computations utilising a finite-element discretisation of the governing Navier–Stokes equations. The results and comparisons reported in Sect. 4 cover both problems of interest. Conclusions are drawn in Sect. 5.

2 Problem specification

The problems of interest, steady, shear- and gravity-driven bilayer flow over a stationary, rigid substrate containing a repeating topographical feature (given by $x_2 = b(x_1)$) and of infinite width, are illustrated in Fig. 1. They involve two immiscible liquids (Newtonian, dynamic viscosity η , and incompressible, density ρ), lying one above the other and separated from each other by an internal interface at $x_2 = f_1(x_1)$.

In the shear-driven case, the confining substrates are in parallel alignment—the upper planar one moving with constant speed u_0 , while for the gravity-driven case, the layers flow down a patterned substrate inclined at a fixed angle to the horizontal. For the latter, both the free-surface shape, as well as that of the internal interface, remain to be determined.

Using tensor notation with Einstein’s summation convention, the general governing continuity and momentum equations for an assumed velocity field, u_i , within the layers are:

$$\partial_i u_i = 0, \quad (1)$$

$$\partial_j [\rho u_j u_i - T_{ij} + \rho V \delta_{ij}] = 0, \quad (2)$$

respectively; $T_{ij} = -p\delta_{ij} + \eta[\partial_i u_j + \partial_j u_i]$ denotes the associated stress tensor and $V = g[x_2 \cos \alpha - x_1 \sin \alpha]$ the specific potential energy.

At the patterned substrate, $x_2 = b(x_1)$, the no-slip/no-penetration condition $u_i(x_1, b(x_1)) = 0$ requires fulfilment. Along the internal interface, $x_2 = f_1(x_1)$, the velocity must remain continuous, $[[u_i]] = 0$ —the double square bracket denoting the jump condition. Additionally, both kinematic, $n_i u_i = 0$, where n_i denotes the normal vector at the interface, and dynamic, $[[T_{ij}]]n_j = [[\sigma]]\kappa n_i$, where $[[\sigma]]$ is the interfacial tension and $\kappa := f_1''(x_1)/\sqrt{1 + f_1'(x_1)^2}$ denotes the curvature, conditions must be fulfilled there.

Depending on the flow type, the boundary conditions at the upper boundary will differ: shear-driven flow requires satisfaction of a no-slip/no-penetration condition there, $u_i(x_1, h_2) = u_0\delta_{1i}$; while for gravity-driven flow, kinematic, $n_i u_i = 0$, and dynamic, $T_{ij}n_j = \sigma_2\kappa n_i$, conditions apply at $x_2 = f_2(x_1)$, where σ_2 is the surface tension. At the left and right boundaries of the flow domains, periodic conditions are assumed to exist.

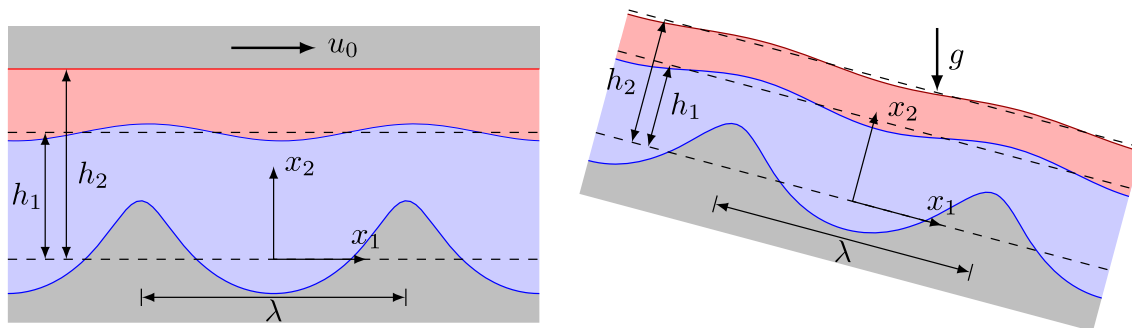


Fig. 1 In-plane schematics of bilayer flow over topography: (i) purely shear-driven (left) and (ii) gravity-driven while open to the atmosphere (right), both taken to be of infinite lateral extent. The geometry is shown for each— h_1 (h_2) represents the mean height of the lower (upper) layer with reference to the mean height of the patterned lower, stationary substrate. u_0 is the speed of the upper confining planar substrate, λ the wavelength of the topography and g the gravitational acceleration which can be ignored in the case of (i)

2.1 Mathematical formulation

2.1.1 Potential-based variational formulation—general case

The continuity equation (1) is fulfilled identically on introduction of a stream function vector Ψ_k , such that:

$$u_i = \varepsilon_{ijk} \partial_j \Psi_k. \tag{3}$$

In an analogous way, the momentum balance (2) is fulfilled identically by introducing a tensor potential, a_{kq} , for the momentum flux density, leading to:

$$\rho u_i u_j - T_{ji} + \rho V \delta_{ij} = \varepsilon_{ikl} \varepsilon_{jpr} \partial_k \partial_p a_{lq}, \tag{4}$$

motivated by an analogy with Maxwell’s theory, see Scholle et al. [13]—for a more detailed treatise the reader is referred to Marner [14]’s thesis.

The most striking advantages of the above is the resulting self-adjoint form achieved, allowing the following Lagrangian [13] for viscous flow to be obtained:

$$\ell = \rho \bar{a}_{ij} u_i u_j + 2[\eta u_j - \partial_j \Phi] \partial_i \bar{a}_{ij} + \frac{1}{2} \varepsilon_{ilk} \varepsilon_{jpr} \partial_i \bar{a}_{ij} \partial_p \bar{a}_{kq}, \tag{5}$$

where the tensor potential is, according to $a_{ij} = \bar{a}_{ij} + 2\Phi \delta_{ij}$, decomposed into traceless, \bar{a}_{ij} and isotropic parts with a scalar potential Φ . The velocity field is expressed in terms of the stream function vector via Eq. (3). The Euler–Lagrange equations resulting by variation of the action integral with respect to \bar{a}_{ij} and Φ , reproduce the tensor field equation (4) by linear combination; whereas, variation with respect to Ψ_i and Φ provides gauging conditions for the potentials [13].

2.1.2 Two-dimensional steady inertialess flow

With reference to the problem specification, the flows of interest are assumed two-dimensional (2D), which is the norm under the assumption that the substrate topography does not vary in the comparably infinite lateral direction. In this case the above general formulation can be adapted accordingly by taking $\Psi_k = \psi \delta_{k3}$ and $\bar{a}_{i3} = 0$ as a specific choice for the stream function vector and the tensor potential, respectively, implying the well-known relationships $u_1 = \partial_2 \psi$, $u_2 = -\partial_1 \psi$ and $u_3 = 0$.

In addition, the layers are taken to be inertialess, hence neglect of the cubic term $\rho \bar{a}_{ij} u_i u_j$ in the Lagrangian (5). The validity of this assumption rests on the Reynolds number being sufficiently small, which for a single fluid layer is generally expressed as $Re = \rho h U / \eta$ where h is the layer thickness and U is the maximum velocity. For a monolayer gravity-driven film the Reynolds number takes the form $Re = \rho^2 g h^3 \sin \alpha / (2\eta^2)$, see Marner et al. [15]. The latter and numerous other studies, for example, by Nguyen and Bontozoglou [16], Aksel and Schörner [17], involving both numerical predictions and experimental observation, reveal the effect of inertia in monolayer films at Reynolds numbers of around 30 and higher. Conversely, for $Re \leq 10$ its effect is negligible. For coating and lubrication flows, $Re \ll 1$ is typical. Additional support for assuming Stokes flow for the problems of interest, is the work of Gaskell et al. [18] and Veremieiev et al. [19], showing that lubrication theory, although not strictly valid above $Re = 0$, produces excellent results for the more challenging case of film flow over steep-sided topography when compared with complementary experimental data [2]. This feature of lubrication theory for small Re when surface patterning is present, is widely accepted within the coating community.

Accordingly, the Euler–Lagrange equations of the Lagrangian (5) with the inertia term neglected, resulting from variation with respect to a_{11} and a_{12} , are:

$$\partial_1(\eta \partial_2 \psi - \partial_1 \Phi) + \partial_2(\eta \partial_1 \psi + \partial_2 \Phi) = 0, \tag{6}$$

$$\partial_2(\eta \partial_2 \psi - \partial_1 \Phi) - \partial_1(\eta \partial_1 \psi + \partial_2 \Phi) = 0. \tag{7}$$

On expressing the velocity in terms of the stream function, the no-slip/no-penetration conditions at the profiled substrate become:

$$\partial_i \psi(x_1, b(x_1)) = 0, \tag{8}$$

one consequence of which is that $\psi(x_1, b(x_1)) = \text{const}$. Since the stream function is thus determined apart from one additional constant, the gauging $\psi(x_1, b(x_1)) = 0$ follows. Similarly, the continuity condition at the internal

interface reads:

$$\llbracket \partial_i \psi(x_1, f_1(x_1)) \rrbracket = 0. \quad (9)$$

A key feature of this potential-based first integral approach, is a greatly simplified expression for the dynamic condition at an internal layer-separating interface, or at a free-surface, namely:

$$\llbracket \partial_i \Phi \rrbracket = \frac{\llbracket \sigma \rrbracket}{2} n_i + \frac{\llbracket \rho \rrbracket}{2} \int V dx_i, \quad (10)$$

for the gradient of the scalar potential [15]. Which, in turn, is an extremely convenient form for obtaining solutions: by decomposition in the tangential and normal directions, the above condition becomes of Dirichlet–Neumann type [15].

The kinematic conditions at the internal interface ($k = 1$) and for gravity-driven flow at the bounding upper free-surface ($k = 2$) also, determining their associated shapes, read:

$$\psi(x_1, f_k(x_1)) = \psi_k = \text{const}. \quad (11)$$

3 Method of solution

Equations (6) and (7) are solved, subject to boundary conditions (8) to (11), using a novel formulation of the complex variable (CV) method for 2D multilayer Stokes flow problems described below, and involves an analytic reduction in dimension (from 2D \rightarrow 1D).

3.1 Complex Variable (CV) method

3.1.1 Analytic formulation and solution of the field equations

Representing the field equations (6) and (7) in terms of the complex variable:

$$\xi := x_1 + ix_2, \quad (12)$$

together with its complex conjugate, $\bar{\xi}$, leads to the following integrable complex equation:

$$\frac{\partial^2}{\partial \xi^2} [\Phi + i\eta\psi] = 0. \quad (13)$$

By direct twofold integration one obtains:

$$\Phi + i\eta\Psi = \bar{\xi}g_0(\xi) + g_1(\xi), \quad (14)$$

containing two holomorphic functions $g_{0,1}(\xi)$, frequently referred to as Goursat functions as, for example, in Mikhlin [20], Scholle et al. [21], requiring determination via the boundary and interface conditions.

The use of holomorphic functions points again to an analogy with the mathematical methods used in Maxwell's theory for the computation of stationary fields, since the general solution (14) fulfils the set of two PDEs, $\nabla^2[\Phi + i\eta\Psi] = 4g_0$ and $\nabla^2 g_0 = 0$, consisting of a Poisson and a Laplace equation. Vice versa, the use of holomorphic functions in classical electrodynamics is widespread and reported in textbooks, for example Jackson [22]. The fact that holomorphic functions fulfil Laplace's equation can be used for their reconstruction from their boundary values by finite differencing—see Sect. 4.3.

3.1.2 Boundary and interface conditions for the CV formulation

For convenience, the notation x is used subsequently in place of x_1 . The lower boundary ($k = 0$), interface ($k = 1$) and upper boundary ($k = 2$) read:

$$\xi = \xi_k(x) := x + ih_k + iH'_k(x),$$

with periodic functions $H'_k(x)$, the period average of which vanishes. These functions indicate the deviation of the local height of the upper boundary of the respective layer from its mean value, h_k . In particular, $H'_0(x) = b(x)$ is the prescribed topographically featured shape of the solid substrate, whereas $H'_1(x)$ denotes the *a priori* unknown shape of the internal interface. In the case of gravity-driven film flows, $H'_2(x)$ denotes the likewise unknown free-surface shape, whereas $H'_2 \equiv 0$ for shear-driven flow. Since the stream function must fulfil periodic boundary conditions only, while the potential Φ may also contain aperiodic terms, the Goursat functions conveniently split into polynomial and periodic parts as in the work of Marner et al. [23] according to:

$$g_0(\xi) = iA\xi + \frac{3C}{4}\xi^2 + iQ(\xi), \tag{15}$$

$$g_1(\xi) = -i\Re A\xi^2 - \frac{C}{4}\xi^3 + 2R(\xi) - i\xi Q(\xi), \tag{16}$$

containing two periodic functions $Q(\xi)$, $R(\xi)$ and two constants, $A \in \mathbb{C}$, $C \in \mathbb{R}$. The no-slip/no-penetration condition (8), multiplied by $\eta_1 \xi'_0(x)$, results in:

$$\frac{d}{dx}[R(\xi_0) + bQ(\xi_0)] + \Im[\bar{\xi}'_0 Q(\xi_0)] = -\left[2\Re Ab + \frac{3}{2}Cb^2\right]\xi'_0. \tag{17}$$

The continuity condition (9) and the dynamic condition (10) can be beneficially combined to form one complex equation, resulting finally in the jump condition:

$$2i[[Q]] = \frac{[[\sigma]]}{2}(n - i) + \frac{[[\varrho]]g}{2}e^{i\alpha} \left[\int H'_1 dx + \frac{i}{2}H_1'^2 \right] + 2i[[\eta]] \frac{\partial \Psi}{\partial \xi} + B, \tag{18}$$

supplemented with $[[A]] = -i[[\varrho]]gh \exp(i\alpha)/4$ and $[[C]] = -[[\varrho]]g \sin \alpha/6$, where $B \in \mathbb{C}$ is an integration constant and $n = n_1 + in_2$ the normal vector. A different linear combination of (9) and (10) leads to a jump condition for R .

The upper boundary condition as the main distinguishing feature between the two flow arrangements is, for the shear-driven flow a no-slip/no-penetration one:

$$\frac{d}{dx}[R(\xi_2) + h_2Q(\xi_2)] + \Im Q(\xi_2) + 2h_2\Re A = u_0; \tag{19}$$

while for gravity-driven film flow a dynamic one applies:

$$\frac{d}{dx}[R + (h_2 + H'_2)Q]_2 - i\Re[\bar{\xi}'_2 Q]_2 = \left[\frac{\varrho g}{4} \left(e^{-i\alpha} \int H'_2 dx - \frac{i}{2}e^{i\alpha} H_2'^2 \right) - \frac{i\sigma}{4}\bar{n} + B \right] \xi'_2, \tag{20}$$

supplemented by the kinematic boundary condition (11) for $k = 2$, determining the free-surface shape.

3.1.3 Spectral discretisation and solution

Subsequently, all lengths are scaled with $\lambda/(2\pi)$, leading to a 2π -periodic problem. The boundary and interface conditions formulated in Sect. 3.1.2 are discretised using a spectral method, making use of Fourier series representations of the form:

$$Q(\xi) = i \sum_{n=-N}^N Q_n \exp(in\xi), \quad R(\xi) = i \sum_{n=-N}^N R_n \exp(in\xi) \tag{21}$$

for the function Q and R , leading to an algebraic set of equations for the respective coefficients Q_n , R_n and for the Fourier coefficients of $H_k(x)$. The resulting nonlinear equation set can be conveniently solved iteratively and was achieved using Python, as in the case of the FE formulation mentioned in Sect. 3.2—further details of which are available in the book chapter Scholle et al. [24] or the thesis by Mellmann [25].

3.2 Comparative methods of solution

In order to highlight the CV method's efficiency, comparisons are also drawn with two further sets of corresponding solutions: the first a purely analytic one based on a long wave approximation applied to the first integral formulation of Navier–Stokes equation [24, 26], referred to here so as to distinguish it from a standard lubrication approximation, as the first integral lubrication method (FL)—see the Appendix; the second involving a finite element (FE) discretisation of the corresponding classical Navier–Stokes equations, solved numerically [24, 25].

4 Results and discussion

4.1 Non-dimensional parameters

By adopting $L = \lambda/(2\pi)$, see Sect. 3.1.3, as a characteristic length scale, the coordinates can be written in dimensionless form as $\tilde{x} = 2\pi x/\lambda$ and $\tilde{y} = 2\pi y/\lambda$, and the dimensionless mean film heights as:

$$\begin{aligned}\tilde{h}_1 &= 2\pi \frac{h_1}{\lambda}, \\ \tilde{h}_2 &= 2\pi \frac{h_2}{\lambda},\end{aligned}$$

and together with the dimensionless amplitude of the substrate:

$$\tilde{a} = \pi \frac{b(\lambda) - b(0)}{\lambda}$$

appear as geometric parameters for both flow configurations. In the case of gravity-driven film flow, the inclination angle α is an additional geometric parameter.

For the sake of simplicity, the tildes above the letters can be dispensed with and \tilde{x} , \tilde{y} and \tilde{h}_1 , \tilde{h}_2 , \tilde{a} , written as x , y and h_1 , h_2 , a , subsequently.

The non-dimensional parameters related to the material properties are the ratios of the viscosities, η_1/η_2 , and densities ρ_1/ρ_2 , while for gravity-driven film flow, the capillary number:

$$\text{Ca} = \frac{\rho_2 g \lambda^2 \sin \alpha}{8\pi^2 \sigma_2}$$

is relevant. If, as in the results which follow, tension at the internal interface is neglected, $[[\sigma]] = 0$ for both flow configurations.

4.2 Comparison of CV and FL results with FE computations for the case of shear-driven flow

For the purpose of demonstrating the benefits of the CV method, comparisons are drawn between solutions obtained using all three methods for the case of a patterned substrate containing harmonic corrugations given by $b(x) = -a \cos x$ with $a = 0.5$.

The corresponding geometry parameters for the two layers are $h_1 = 0.7$ and $h_2 = 1.3$. Two viscosity ratios, $\eta_1/\eta_2 = 2$ and $1/2$ are considered, with $\rho_1/\rho_2 = 1$. All three predictions reveal flow separation to occur. While the FL results capture the main features of the flow, those obtained using the CV method compare almost identically with the corresponding high-fidelity FE ones—but with the former generated in a fraction of the computational time: the CV computations of Fig. 2 taking approximately 0.24s of CPU time on MacBook Pro, M1 processor, 8 GB memory; while the corresponding FE ones took approximately 250s of CPU time—a factor of the order of 1000 times greater. Both methods were implemented using Python 3.9.

The samples shown here also confirm the reliability of the CV method, which has already been validated for monolayer flows via comparisons with both numerical results and experimentally obtained flow visualisations by, for example, Aksel and Schörner [27], Marner et al. [23], Scholle et al. [17].

The FL method, although less accurate than the CV and FE approaches, which produce comparable results, nevertheless proves itself to be a very useful and cheap tool for quickly identifying the rudimentary features of both flow arrangements worthy of a more detailed and accurate investigation using one of the other two solvers.

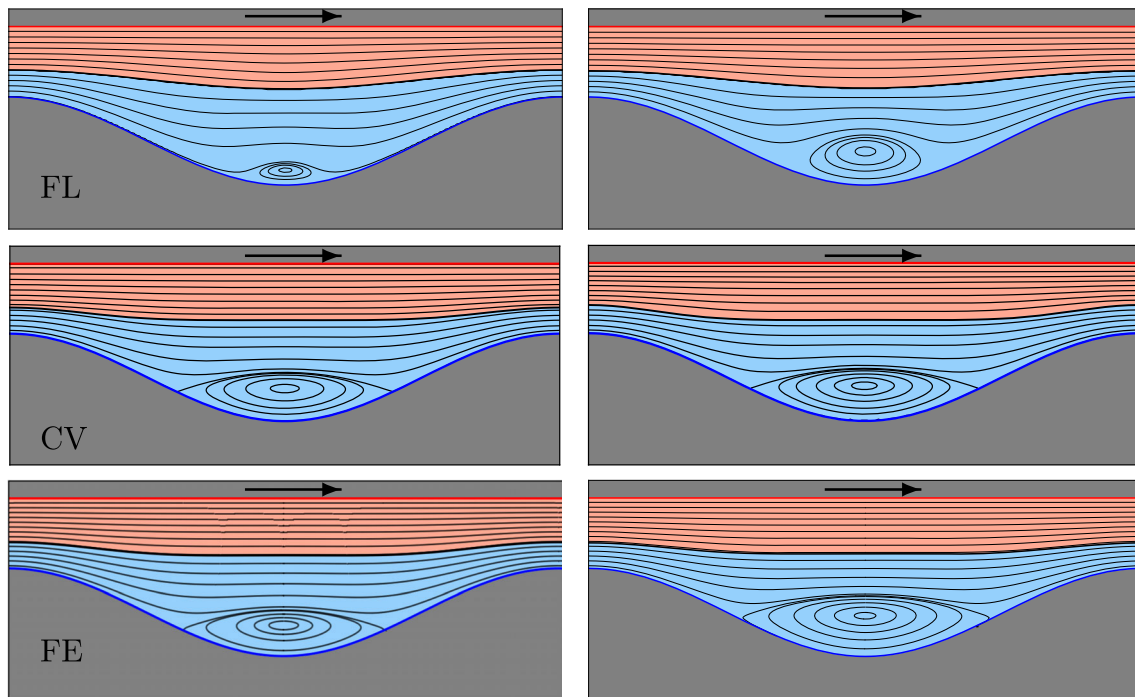


Fig. 2 Streamline flow patterns for bilayer inertialess shear-driven flow, as predicted by the FL (top), CV (middle) and FE (bottom) methods of solution: $a = 0.5$, $\eta_1/\eta_2 = 2$ (left) and $\eta_1/\eta_2 = 1/2$ (right). The upper planar substrate is moving from left to right, consistent with Fig. 1

The efficacy of the CV method having been established for shear-driven flow when predictions are compared to their high-fidelity FE counterparts, the subsequent need to generate FL and FE solutions for comparison purposes is now dispensed with.

4.3 Gravity-driven flow over weak surface undulations

Based on the above results, the CV method alone is now used to solve for bilayer gravity-driven flow over harmonic corrugations; first for the case of comparatively small amplitude $a = 0.3$.

Figure 3 shows results for the internal flow structure within both layers for four different angles, α , of inclination to the horizontal of the rigid substrate shaded grey. The geometrical values are $a = 0.3$, $h_1 = 0.7$, $h_2 = 1.3$, the capillary number, $Ca = 1$, and the ratio of the fluid properties $\rho_1/\rho_2 = 1$, $\eta_1/\eta_2 = 1/3$. The component of gravity acting in the direction of flow increases with inclination angle, revealing that the free-surface minimum, indicated by the vertical arrow pair, shifts to the upstream side the lower the value of α , accompanied by a corresponding increased free-surface disturbance recognisable by the peak-to-peak amplitude indicated again by the vertical arrow pair.

In Fig. 4 a change in the value of the surface tension at the upper free-surface is investigated for a substrate inclination angle of $\alpha = 60^\circ$, keeping the other parameters the same. For the smaller of the two Ca values there is a clear smoothing of the surface tension effect and hence a decrease in the disturbance there. This is consistent with what is found for single layer flows with the obvious outcome that in the limit of $Ca \rightarrow 0$ the free-surface would be planar.

4.4 Gravity-driven flow over strong surface undulations

The CV method as presented above is restricted to amplitudes $a \leq 0.5$, since for larger values the Fourier series (21) diverges, which is well known from prior investigations by Scholle et al. [27], Malevich et al. [28]. This shortcoming can be satisfactorily addressed and overcome by various strategies: a Padé approximation replacing the divergent Fourier series is used by Malevich et al. [28]; while Scholle et al. [27] utilise, and as adopted here, a local Fourier

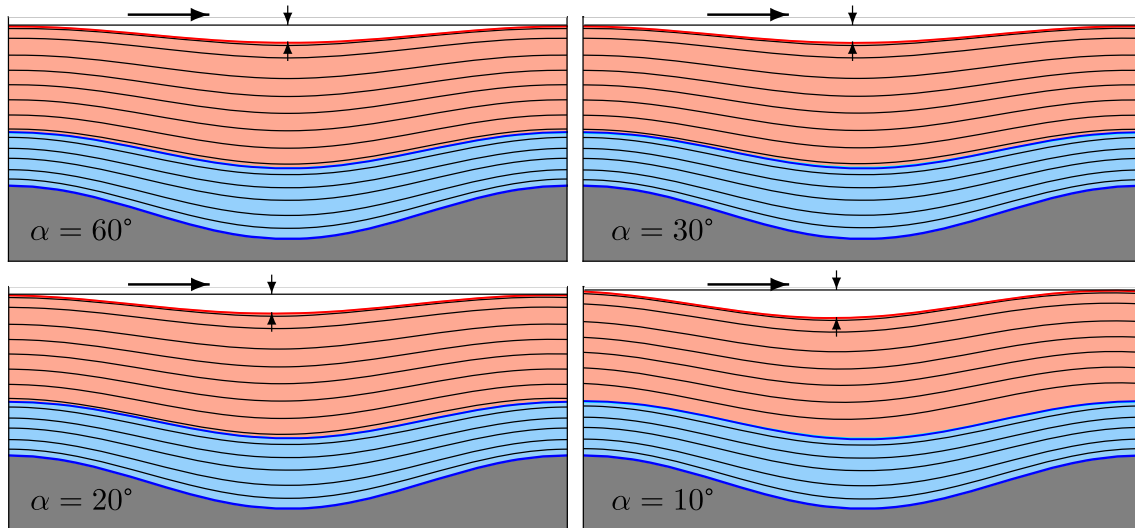


Fig. 3 Bilayer gravity-driven film flow: streamlines for the case $a = 0.3$, $h_1 = 0.7$, $h_2 = 1.3$, $\varrho_2/\varrho_1 = 1$, $Ca = 1$, $\eta_1/\eta_2 = 1/3$ for different inclination angles of the profiled substrate. The flow is from left to right as indicated by the large single arrow, while the vertical arrow pairs indicate both the position of the surface minimum and the peak-to-peak amplitude of the free-surface disturbance

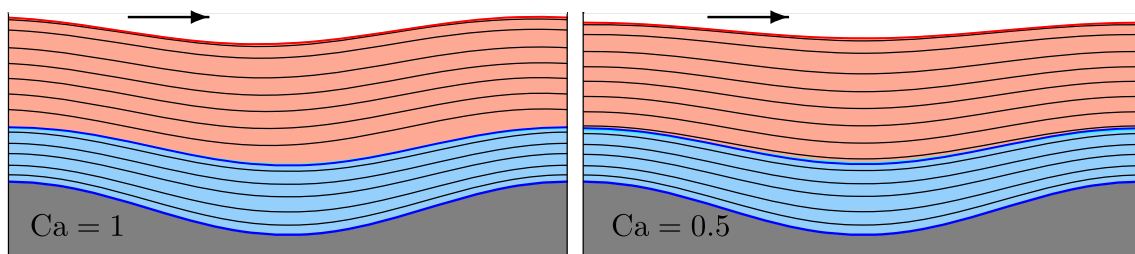


Fig. 4 Bilayer gravity-driven film flow: streamlines for $a = 0.3$, $h_1 = 0.7$, $h_2 = 1.3$, $\varrho_2/\varrho_1 = 1$, $\eta_1/\eta_2 = 1/3$, for the case when the profiled substrate is at an angle $\alpha = 60^\circ$, and for two different capillary numbers. The flow is from left to right as indicated by the large arrow

discretisation according to:

$$Q^\pm(\xi_k(x)) = i \sum_{m=-N}^N q_{k,m}^\pm \exp(imx), \quad (22)$$

for the boundary values of Q above (+) and below (−) the k -th boundary line. The same applies to R . The functions Q and R themselves are reconstructed via a second step, from their boundary values, which in the present work is achieved via finite differencing of the Laplace equation. This additional numerical step requires some additional CPU time¹, but is only necessary for the visualisation of the streamlines, while, for example, the free-surface shape can be determined without the need for reconstructing the values of the holomorphic functions inside the flow domain.

Exemplary results, obtained using the above methodology, for varying viscosity ratio η_2/η_1 , $Ca = 1$ and a substrate inclination angle of $\alpha = 45^\circ$, are shown in Fig. 5. In all cases the upper free-surface is essentially planar due to the thickness of the upper layer compared to the lower one. However, while the curvature of the internal interface is found to be influenced only slightly by a change in the viscosity ratio, the size and extent of the eddy structure present depends strongly on it.

¹Typically ≈ 10 s for the samples shown in Fig. 5 using the same hardware and Python version as reported in Sect. 4.1.

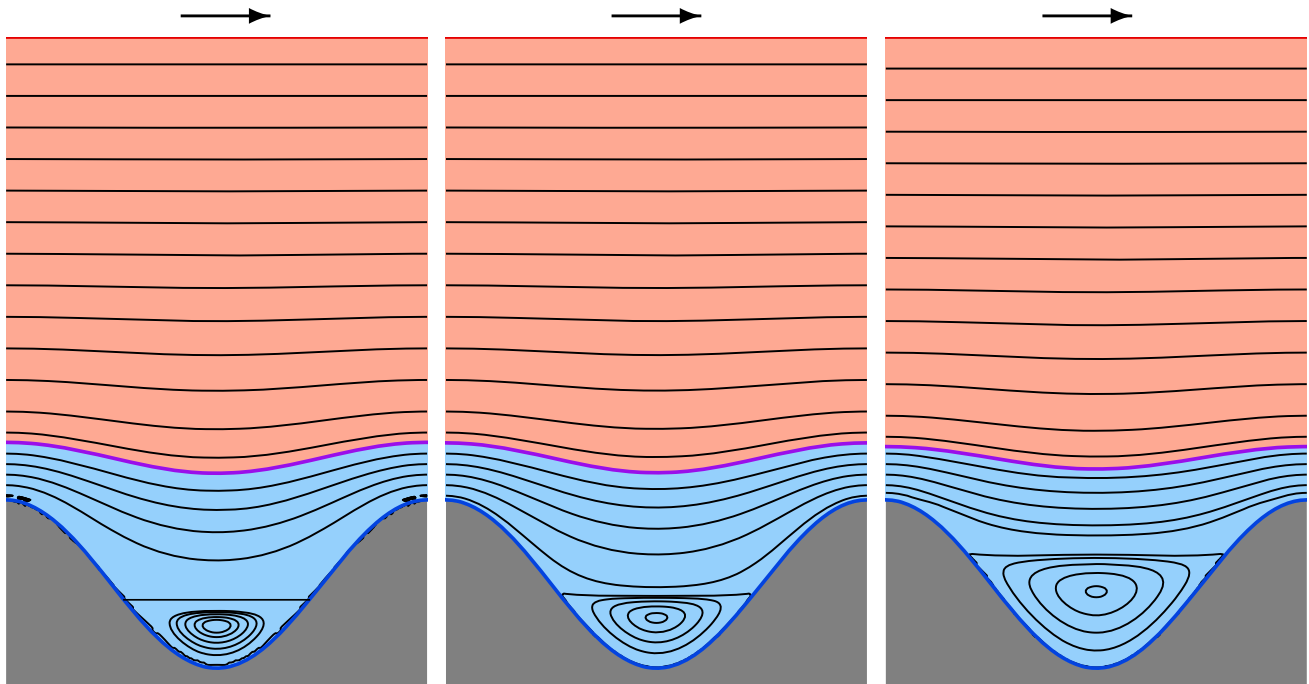


Fig. 5 Bilayer gravity-driven film flow: streamlines with $a = 1.257$, $h_1 = 1.885$, $h_2 = 8.168$, $\rho_2/\rho_1 = 1$, and $Ca = 1$ for the case when the profiled substrate is at an angle $\alpha = 45^\circ$, and for three different viscosity ratios $\eta_2/\eta_1 = 0.9$ (left), $\eta_2/\eta_1 = 1$ (middle) and $\eta_2/\eta_1 = 2$ (right). The flow is from left to right as indicated by the large arrow

5 Concluding remarks

The potential-based first integral approach adopted provides a promising basis for the development of highly efficient analytical (FL) and semi-analytical (CV) solution methods for the exploration of multilayer lubrication like and related coating flow problems in the Stokes flow limit. Its major benefits are the existence of a variational principle and a considerably simplified form of the dynamic interface condition to a Dirichlet/Neumann form.

Apart from the efficiency of the CV method, allowing solutions to be generated in a mere fraction of the time required to produce equivalent high-fidelity FE solutions of the corresponding full Navier-Stokes equations for incompressible flow, their beneficial representation in terms of Fourier series promotes their use as base-flow solutions for a subsequent stability analysis; the latter forming the topic of a forthcoming investigation making use of a more general first integral formulation developed by Marner et al. [23] for unsteady 2D flow with inertia. In addition it would be a relatively straight forward matter to extend the above investigations to the case of non-Newtonian liquids.

Likewise, more demanding 3D related flow problems, see Veremieiev et al. [29] and D'Alessio [30], can be addressed as future research, which is clear from the potential-based variation formulation shown in its general form in Sect. 2.1.1.

Funding Open Access funding enabled and organized by Projekt DEAL.

Open Access This article is licensed under a Creative Commons Attribution 4.0 International License, which permits use, sharing, adaptation, distribution and reproduction in any medium or format, as long as you give appropriate credit to the original author(s) and the source, provide a link to the Creative Commons licence, and indicate if changes were made. The images or other third party material in this article are included in the article's Creative Commons licence, unless indicated otherwise in a credit line to the material. If material is not included in the article's Creative Commons licence and your intended use is not permitted by statutory regulation or exceeds the permitted use, you will need to obtain permission directly from the copyright holder. To view a copy of this licence, visit <http://creativecommons.org/licenses/by/4.0/>.

Appendix A. Analytical first integral lubrication (FL) method of solution

Invoking the long-wave (lubrication) approximation, see Oron et al. [31], Craster and Matar [32], based on the assumptions that (i) the flow velocity u_1 in the direction of flow dominates compared to the velocity in the cross-flow direction, u_2 , while (ii) gradients in the cross-flow direction are dominant compared to those in direction of flow, namely $\partial_1^2\psi \ll \partial_2^2\psi$, simplifies the field equation (7) to the integrable form $\partial_2[\eta u_1 - 2\partial_1\Phi] = 0$, which following integration yields:

$$2\partial_1\Phi = \eta u_1 + F_1(x_1), \quad (\text{A1})$$

containing the function $F_1(x_1)$. substituting the above into Eq. (6), results once more in an integrable form, which following integration, leads to:

$$2\partial_2\Phi = 3\eta u_2 + F_1'(x_1)x_2 + F_2(x_1), \quad (\text{A2})$$

giving rise to a second integration function $F_2(x_1)$. After elimination of the potential Φ by computing $\partial_2(\text{A1}) - \partial_1(\text{A2})$ and further integration steps, one finally obtains the following analytical solution—see [24] for the stream function:

$$\eta\psi = F_1''(x_1)\frac{x_2^3}{6} + F_2'(x_1)\frac{x_2^2}{2} + F_3(x_1)x_2 + F_4(x_1). \quad (\text{A3})$$

The integration functions $F_1(x_1), \dots, F_4(x_1)$ are obtained by inserting the above solution into the boundary and interface conditions. This procedure is explained in detail by Scholle et al. [26] for a monolayer film flow and applied to bilayer shear-driven flow in the book chapter Scholle et al. [24].

References

1. L.E. Stillwagon, R.G. Larson, Leveling of thin films over uneven substrates during spin coating. *Phys. Fluids A* **2**(11), 1937–1944 (1990). <https://doi.org/10.1063/1.857669>
2. M.M. Decré, J.-C. Baret, Gravity-driven flows of viscous liquids over two-dimensional topographies. *J. Fluid Mech.* **487**, 147–166 (2003). <https://doi.org/10.1017/S0022112003004774>
3. Y.C. Lee, H.M. Thompson, P.H. Gaskell, Filmpar: a parallel algorithm designed for the efficient and accurate computation of thin film flow on functional surfaces containing micro-structure. *Comput. Phys. Commun.* **180**(12), 2634–2649 (2009). <https://doi.org/10.1016/j.cpc.2009.06.012>. (40 YEARS OF CPC: A celebratory issue focused on quality software for high performance, grid and novel computing architectures)
4. A.A. Abdalla, S. Veremieiev, P.H. Gaskell, Steady bilayer channel & free-surface isothermal film flow over topography. *Chem. Eng. Sci.* **181**, 215–236 (2018). <https://doi.org/10.1016/j.ces.2018.01.031>
5. J. Thompson, M.G. Blyth, Inertialess multilayer film flow with surfactant: stability and traveling waves. *Phys. Rev. Fluids* **1**, 063904 (2016). <https://doi.org/10.1103/PhysRevFluids.1.063904>
6. J.P. Alexander, D.T. Papageorgiou, Ordered and disordered dynamics in inertialess stratified three-layer shear flows. *Phys. Rev. Fluids* **7**, 014804 (2022). <https://doi.org/10.1103/PhysRevFluids.7.014804>
7. M. Qiu, A. Chyr, A.P. Sanders, B. Raeymaekers, Designing prosthetic knee joints with bio-inspired bearing surfaces. *Tribol. Int.* **77**, 106–110 (2014). <https://doi.org/10.1016/j.triboint.2014.04.025>
8. H. Basri, A. Syahrom, T.S. Ramadhoni, A.T. Prakoso, M.I. Ammarullah, Vincent: the analysis of the dimple arrangement of the artificial hip joint to the performance of lubrication. *IOP Conf. Ser. Mater. Sci. Eng.* **620**, 012116 (2019). <https://doi.org/10.1088/1757-899x/620/1/012116>
9. D. Nečas, H. Usami, T. Niimi, Y. Sawae, I. Krupka, M. Hartl, Running-in friction of hip joint replacements can be significantly reduced: the effect of surface-textured acetabular cup. *Friction* (2020). <https://doi.org/10.1007/s40544-019-0351-x>
10. C. Gachot, A. Rosenkranz, S.M. Hsu, H.L. Costa, A critical assessment of surface texturing for friction and wear improvement. *Wear* **372–373**, 21–41 (2017). <https://doi.org/10.1016/j.wear.2016.11.020>
11. A. Chyr, M. Qiu, J.W. Speltz, R.L. Jacobsen, A.P. Sanders, B. Raeymaekers, A patterned microtexture to reduce friction and increase longevity of prosthetic hip joints. *Wear* **315**(1), 51–57 (2014). <https://doi.org/10.1016/j.wear.2014.04.001>
12. S.F. Kistler, P.M. Schweitzer (eds.), *Liquid Film Coating* (Chapman & Hall, London, 1997)
13. M. Scholle, P.H. Gaskell, F. Marner, Exact integration of the unsteady incompressible Navier–Stokes equations, gauge criteria, and applications. *J. Math. Phys.* **59**(4), 043101 (2018). <https://doi.org/10.1063/1.5031119>
14. F. Marner, Potential-based formulations of the Navier–Stokes equations and their application. PhD thesis, Durham University, Durham, UK (2019). <http://etheses.dur.ac.uk/13270/1/>

15. F. Marner, P.H. Gaskell, M. Scholle, On a potential-velocity formulation of Navier–Stokes equations. *Phys. Mesomech.* **17**(4), 341–348 (2014). <https://doi.org/10.1134/S1029959914040110>
16. P.-K. Nguyen, V. Bontozoglou, Steady solutions of inertial film flow along strongly undulated substrates. *Phys. Fluids* **23**(5), 052103 (2011). <https://doi.org/10.1063/1.3591154>
17. N. Aksel, M. Schörner, Films over topography: from creeping flow to linear stability, theory, and experiments, a review. *Acta Mech.* **229**(4), 1453–1482 (2018). <https://doi.org/10.1007/s00707-018-2146-y>
18. P.H. Gaskell, P.K. Jimack, M. Sellier, H.M. Thompson, M.C.T. Wilson, Gravity-driven flow of continuous thin liquid films on non-porous substrates with topography. *J. Fluid Mech.* **509**, 253–280 (2004). <https://doi.org/10.1017/S0022112004009425>
19. S. Veremieiev, H.M. Thompson, Y.C. Lee, P.H. Gaskell, Inertial thin film flow on planar surfaces featuring topography. *Comput. Fluids* **39**(3), 431–450 (2010). <https://doi.org/10.1016/j.compfluid.2009.09.007>
20. S.G. Mikhlin, *Integral Equations and Their Applications to Certain Problems in Mechanics. Mathematical Physics and Technology* (Pergamon Press, NY, 1957)
21. M. Scholle, F. Marner, P.H. Gaskell, Potential fields in fluid mechanics: a review of two classical approaches and related recent advances. *Water* (2020). <https://doi.org/10.3390/w12051241>
22. J.D. Jackson, *Classical Electrodynamics*, 3rd edn. (Wiley, New York, 1999)
23. F. Marner, P.H. Gaskell, M. Scholle, A complex-valued first integral of Navier–Stokes equations: unsteady Couette flow in a corrugated channel system. *J. Math. Phys.* **58**(4), 043102 (2017). <https://doi.org/10.1063/1.4980086>
24. M. Scholle, M. Mellmann, P.H. Gaskell, L. Westerkamp, F. Marner, Multilayer modelling of lubricated contacts—a new approach based on a potential field description. In: Ostermeyer, G.-P., Popov, V.L., Shilko, E.V., Vasiljeva, O. (eds.) *Multiscale Biomechanics and Tribology of Inorganic and Organic Systems—In Memory of Professor Sergey Psakhie*. Springer Tracts in Mechanical Engineering. Springer, Berlin (2021). https://doi.org/10.1007/978-3-030-60124-9_16
25. M. Mellmann, Simulation dünner Filme mit freien Oberflächen u. Phasengrenzen mittels eines iterativen FE-Verfahrens. Master’s thesis, Heilbronn Univ. (2020)
26. M. Scholle, P.H. Gaskell, F. Marner, A potential field description for gravity-driven film flow over piece-wise planar topography. *Fluids* **4**(2), 82 (2019). <https://doi.org/10.3390/fluids4020082>
27. M. Scholle, A. Wierschem, N. Aksel, Creeping films with vortices over strongly undulated bottoms. *Acta Mech.* **168**(3), 167–193 (2004). <https://doi.org/10.1007/s00707-004-0083-4>
28. A.E. Malevich, V.V. Mityushev, P.M. Adler, Stokes flow through a channel with wavy walls. *Acta Mech.* **182**(3–4), 151–182 (2006). <https://doi.org/10.1007/s00707-005-0293-4>
29. S. Veremieiev, H.M. Thompson, P.H. Gaskell, Free-surface film flow over topography: full three-dimensional finite element solutions. *Comput. Fluids* **122**, 66–82 (2015). <https://doi.org/10.1016/j.compfluid.2015.08.016>
30. S.J.D. D’Alessio, A new ibl model for quasi-unidirectional gravity-driven flow over topography. *Eur. J. Mech. B. Fluids* **102**, 18–30 (2023). <https://doi.org/10.1016/j.euromechflu.2023.07.004>
31. A. Oron, S.H. Davis, S.G. Bankoff, Long-scale evolution of thin liquid films. *Rev. Mod. Phys.* **69**, 931–980 (1997). <https://doi.org/10.1103/RevModPhys.69.931>
32. R.V. Craster, O.K. Matar, Dynamics and stability of thin liquid films. *Rev. Mod. Phys.* **81**, 1131–1198 (2009). <https://doi.org/10.1103/RevModPhys.81.1131>